Microscopic origin of magnetism in monolayer 3*d* transition metal dihalides

Kira Riedl [1,*,†] Danila Amoroso [2,3,*,‡] Steffen Backes [4] Aleksandar Razpopov,[1] Thi Phuong Thao Nguyen [5,6]
Kunihiko Yamauchi [5,6] Paolo Barone [7] Stephen M. Winter,[8] Silvia Picozzi,[2] and Roser Valentí [1]

[1]*Institut für Theoretische Physik, Goethe-Universität Frankfurt, Max-von-Laue-Strasse 1, 60438 Frankfurt am Main, Germany*
[2]*Consiglio Nazionale delle Ricerche CNR-SPIN, c/o Universitá degli Studi'G. D'Annunzio', 66100, Chieti, Italy*
[3]*NanoMat/Q-mat/CESAM,Université de Liège, B-4000 Liège, Belgium*
[4]*CPHT, CNRS, Ecole Polytechnique, Institut Polytechnique de Paris, Route de Saclay, 91128 Palaiseau, France, F-91128 Palaiseau, France
Collége de France, 11 place Marcelin Berthelot, 75005 Paris, France European Theoretical Spectroscopy Facility, 91128 Palaiseau, France*
[5]*Institute of Scientific and Industrial Research ISIR-SANKEN, Osaka University, 8-1 Mihogaoka, Ibaraki, Osaka 567-0047, Japan*
[6]*Department of Precision Engineering, Graduate School of Engineering, Osaka University, 2-1 Yamadaoka, Suita, Osaka 565-0871, Japan*
[7]*Consiglio Nazionale delle Ricerche CNR-SPIN, Area della Ricerca di Tor Vergata,Via del Fosso del Cavaliere 100, I-00133 Rome, Italy*
[8]*Department of Physics and Center for Functional Materials, Wake Forest University, Winston-Salem, North Carolina 27109, USA*

Motivated by the recent wealth of exotic magnetic phases emerging in two-dimensional frustrated lattices, we investigate the origin of possible magnetism in the monolayer family of triangular lattice materials MX_2 (M=V, Mn, Ni and X=Cl, Br, I). We first show that consideration of general properties such as filling and hybridization enables to formulate the trends for the most relevant magnetic interaction parameters. In particular, we observe that the effects of spin-orbit coupling (SOC) can be effectively tuned through the ligand elements as the considered 3*d* transition metal ions do not strongly contribute to the anisotropic component of the intersite exchange interaction. Consequently, we find that the corresponding SOC matrix elements differ significantly from the atomic limit. In the next step and by using two *ab initio* based complementary approaches, we extract realistic effective spin models and find that in the case of heavy ligand elements, SOC effects manifest in anisotropic exchange and single-ion anisotropy only for specific fillings.

I. INTRODUCTION

Transition-metal-based materials with magnetically frustrated lattices have been at the center of intensive research for several decades [1–6] due to the presence of fascinating phases ranging from unconventional ordered states to spin liquids. In recent years, two-dimensional (2D) van der Waals magnets have emerged as a new platform for exotic magnetism in reduced dimensions. One of the most prominent examples is the honeycomb spin-1/2 α-RuCl$_3$ which has dominant frustrating Kitaev interactions [7–13] as a result of an interplay of crystal field splitting, Coulomb repulsion and spin-orbit coupling of Ru 4*d* electrons. Anisotropic exchange interactions are also being discussed in the context of 2D van der Waals magnets with 3*d* transition metals, such as the spin-3/2 CrI$_3$, where SOC effects arise from the ligand iodine mediating the exchange; nevertheless, the underlying physics and strength of such interactions still remain rather controversial [14–22].

Motivated by the significance of understanding the origin of mechanisms behind the different magnetic interactions in 2D van der Waals (vdW) magnets, we study here the case of magnetic exchange interactions of selected monolayer 3*d*

transition metal dihalides MX_2 (M=V, Mn, Ni and X=Cl, Br, I), where the cations M are in the octahedral environment of the ligand X anions, and are arranged in a triangular lattice, as depicted in Fig. 1(a). These materials exhibit a variety of interesting properties. For example, type-II multiferroicity was reported in bulk NiBr$_2$ [23], NiI$_2$ [24], and MnI$_2$ [25,26], where the onset of helimagnetic phases breaks inversion symmetry leading to spin-induced ferroelectricity. Such a multiferroic phase has been recently reported to survive down to the monolayer limit of NiI$_2$ [27,28], while monolayer NiBr$_2$ and NiCl$_2$ have been proposed as half-excitonic insulators [29]. The electronic structure of the 3*d* MX_2 compounds has been recently analyzed [30,31]; however, the magnetic exchange couplings and SOC-driven anisotropic contributions have not been fully addressed and require deeper investigation.

The purpose of the present work is twofold: (i) to uncover the microscopic mechanism behind the magnetic couplings in the 2D dihalides with 3*d* transition metals and (ii) to benchmark two complementary *ab initio* approaches for the estimation of magnetic couplings, the "projED" [32] and "four-state" [33,34] methods. The selected materials allow us to address the underlying processes behind the magnetic couplings by studying the influence of different electron filling through the metal elements M, and the effective spin-orbit coupling (SOC) through the ligand elements X, as schematically shown in Fig. 1(b). The magnetic properties of the respective materials can be then generally described in terms

*These authors contributed equally to this work.

†riedl@itp.uni-frankfurt.de
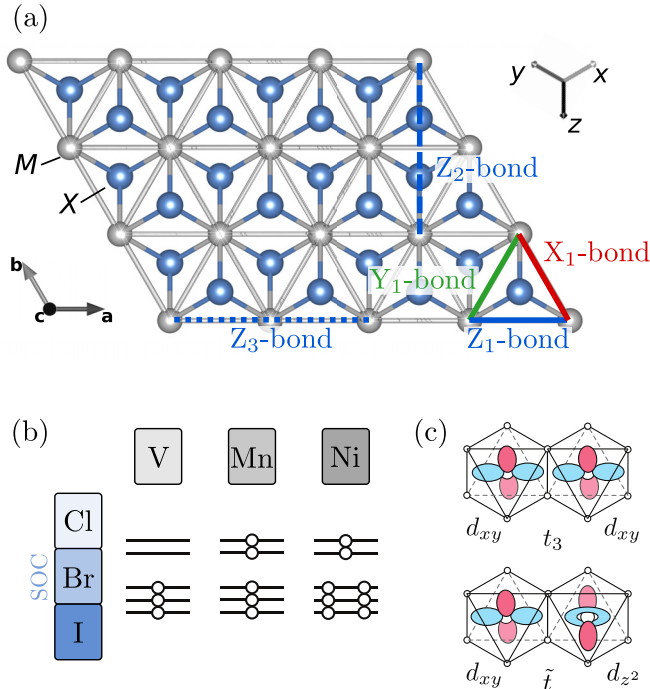
‡danila.amoroso@uliege.be

(a)

(b)

(c)

FIG. 1. (a) Common structure of the triangular MX_2 materials, for which monolayer structures are investigated in this work. Relevant bonds, the crystallographic (abc) coordinate system and the cubic (xyz) coordinate system are defined. (b) Filling for VX_2, MnX_2, and NiX_2 with $X =$ Cl, Br, and I. A darker color illustrates higher filling (grey) or stronger SOC (blue). (c) Dominant hoppings t_3 and $\tilde{t}$ on a nearest-neighbor Z_1 bond.

of effective (anisotropic) spin Hamiltonians with $S = \{3/2, 5/2, 1\}$, dependent on the filling $\{d^3, d^5, d^8\}$.

The paper is organized as follows; in Secs. II and III, we discuss the spin model and general trends for the magnetic exchange couplings in MX_2 considering crystal-field splittings and the Goodenough-Kanamori-Anderson rules [35,36]. In Sec. IV, we present our results on the *ab initio* estimated magnetic interactions and discuss the resulting magnetic properties for the dihalide family. In Sec. V, we present our conclusions.

II. SPIN MODEL

The most general spin Hamiltonian model, including single-ion anisotropy $\mathbb{A}_l$ and bilinear exchange tensors $\mathbb{J}_{lm}$ (with sites l, m), is given by

$$\mathcal{H} = \sum_l \mathbf{S}_l \cdot \mathbb{A}_l \cdot \mathbf{S}_l + \sum_{<lm>} \mathbf{S}_l \cdot \mathbb{J}_{lm} \cdot \mathbf{S}_m. \quad (1)$$

For convenience, we express the single-ion anisotropy (SIA) in the crystallographic coordinate system (ab^*c), where b^* is perpendicular to the ac crystal axes, $\mathcal{H}_{\text{SIA}} = A_c \sum_l (S_l^c)^2$ consistently with the symmetry of MX_2. This allows us to easily identify the triangular layer as an easy or hard plane. On the other hand, the bond-dependent bilinear exchange parameters are most conveniently described in the cubic coordinate system (xyz), which consists of orthogonalized axes oriented approximately along M-X bonds, as illustrated in Fig. 1(a).

Note that the M-X bonds are not perfectly orthogonal due to trigonal distortion effects.

Within the $P\bar{3}m1$ space group (164), to which the centrosymmetric monolayer structures belong, the bilinear exchange coupling matrix has four independent parameters. Here, we adopt a bond-dependent parametrization corresponding to the extended Heisenberg-Kitaev model [37,38]. In this framework, each bond is labeled after the cubic axis perpendicular to it. For a nearest-neighbor Z_1 bond, perpendicular to the z axis [Fig. 1(a)], the exchange couplings are then conventionally parametrized as follows:

$$\mathbb{J}_{lm} = \begin{pmatrix} J & \Gamma & \Gamma' \\ \Gamma & J & \Gamma' \\ \Gamma' & \Gamma' & J + K \end{pmatrix} \quad (2)$$

with the bond-isotropic Heisenberg exchange J, the anisotropic Kitaev exchange K, and the off-diagonal symmetric exchange terms Γ and Γ'; particularly, from now on, we will refer with J_1, J_2, and J_3 to the first, second, and third neighbor Heisenberg interactions. This is the most symmetric general expression for the exchange tensor given the crystal symmetries that enforce four independent parameters. The bilinear exchange matrices for the X and Y bonds are related to Eq. (2) by C_3 rotation about the out-of-plane axis. A correspondence to a parametrization oriented along the crystallographic axes coordinate system (ab^*c) is given in Appendix A.

III. GENERAL CONSIDERATIONS

We start by identifying general traits in hybridization patterns and fillings in $3d$-MX_2 triangular lattice compounds, with edge-sharing halogen ligand octahedra. As we discuss below, this will allow us to formulate trends for the most relevant magnetic interactions.

A. Metal-ligand hybridization

The hybridization between the metal d and ligand p orbitals is generally expected to increase as the electronegativity difference between the two elements decreases. This affects related electronic properties, such as the local Coulomb repulsion U_{avg}, the strength of different hopping processes and the materials' SOC matrix elements. These factors all together ultimately determine the magnetic couplings.

We quantify the hybridization in MX_2 via non-spin-polarized density functional theory (DFT) calculations, through the generalized gradient approximation (GGA) [39] orbital-resolved density of states (DOS). In particular, the energy window dominated by p-d bonding orbitals contains also a finite d character that scales with the degree of hybridization. This is illustrated for the example case of VCl_2 in Fig. 2(b), where a finite d character (in blue) is present within the relevant energy window (marked by the grey box). The integral of the metal $3d$ DOS in the respective p-d bonding dominated energy window is shown for each material in Fig. 2(c). As expected, the hybridization increases with smaller electronegativity difference, i.e., for each of the considered metal elements it increases with ligand atomic number. For the NiX_2
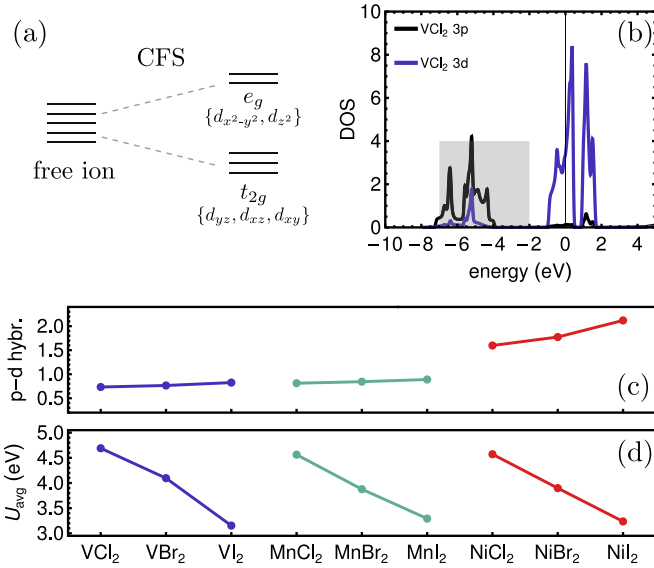
FIG. 2. (a) Cubic crystal-field splitting (CFS) of d orbitals into t_{2g} and e_g levels, (b) *ab initio* (GGA) density of states (DOS) of VCl_2, (c) p-d hybridization, i.e., integral of $3d$ DOS in the energy region dominated by p-d bonding [illustrated by the grey box in (b)], and (d) U_{avg} calculated with cRPA for each MX_2 material.

systems, an especially strong hybridization is observed due to the larger electronegativity of nickel.

To estimate trends in the effective Coulomb interaction U_{avg}, we employed the constrained random-phase approximation (cRPA) [40,41], detailed in Appendix B. The results for each material are given in Table I, and U_{avg} is illustrated in Fig. 2(d). We observe a decrease of U_{avg} as a function of ligand atomic number, which can be related to the increasing metal-ligand hybridization [see Fig. 2(c)]. Accordingly, we find the smallest effective interaction parameters for the strongest hybridizing, and hence most delocalized, orbitals. We have taken the cRPA values of the effective Coulomb repulsion U_{avg} and Hund's coupling J_{avg} as input modeling parameters to estimate the magnetic interaction parameters by means of the two *ab initio* methods (Sec. IV).

B. Nearest-neighbor isotropic exchange interactions

In general, there are various exchange processes that are relevant to the magnetic couplings. The trends for different ligands and filling can be rationalized by considering effective d-d hopping integrals estimated via Wannier projection [42,43] onto a d-only basis. In this section, we work within the cubic CFS framework, depicted in Fig. 2(a),

TABLE I. Constrained RPA results of averaged Hubbard repulsion U_{avg} (in eV) and averaged Hund's coupling J_{avg} (in eV) for the monolayer structures of each investigated material.

	VX_2			MnX_2			NiX_2		
X	Cl	Br	I	Cl	Br	I	Cl	Br	I
U_{avg}	4.69	4.10	3.15	4.56	3.88	3.29	4.57	3.90	3.24
J_{avg}	0.65	0.63	0.57	0.79	0.75	0.71	0.84	0.79	0.68

although in the real materials trigonal distortion leads to additional small splitting within the t_{2g} orbitals. With the zeroth order angular momentum absent in the filled t_{2g} orbitals, the trigonal splitting may be neglected for the sake of simplicity. The *ab initio* results discussed in Sec. IV, on the other hand, consider the full crystal structure and with that also the distortion effects. Precise hopping parameters estimated using nonrelativistic DFT calculations with the full potential local orbital (FPLO) [44][1] basis as well as complete expressions for symmetry-allowed hopping matrices are given in Appendix C. An alternative analysis, based on spin-polarized Wannier projection is detailed in Appendix D.

Over the entire series of materials, we find that the dominant nearest-neighbor hoppings are t_3 and $\tilde{t}$; on the Z_1 bond, for example, these correspond to $t_{(xy;xy)}$ and $t_{(xy,z^2)}$, respectively, illustrated in Fig. 1(c). For the ideal 90° M-X-M bond geometry, t_3 is mainly the result of direct overlap, while $\tilde{t}$ has contributions from both direct hopping and ligand hybridization (with the latter dominating). Consequently, $\tilde{t}$ becomes increasingly important as the p-d hybridization increases.

The consequences of the dominant d-d hopping parameters t_3 and $\tilde{t}$ on the magnetic interactions can be understood in terms of filling of the t_{2g} or e_g orbitals [see Fig. 2(a)] according to the Goodenough-Kanamori-Anderson (GKA) rules [35,36]. In particular, hopping between half-filled orbitals is associated with antiferromagnetic exchange, while hopping from a half-filled to a full or empty orbital is associated with ferromagnetic exchange.

For the d^8 materials (i.e., NiX_2), we generally expect the nearest-neighbor couplings to be ferromagnetic: the t_{2g} levels are filled; hence, the hopping processes involving t_3 do not contribute to exchange in lowest order. Therefore J_1 arises mainly from $\tilde{t}$ processes, which connect a half-filled e_g orbital to a filled t_{2g} orbital, and leads to a ferromagnetic exchange. This effect is enhanced in systems with heavier ligands, as the ligand-assisted $\tilde{t}$ is strengthened by increased p-d hybridization.

For the d^3 materials (i.e., VX_2), there is a competition between ferromagnetic (FM) and antiferromagnetic (AFM) contributions to the nearest-neighbor exchange. In addition to the ferromagnetic exchange arising from the $\tilde{t}$ process connecting an empty e_g with a half-filled t_{2g} orbital, an antiferromagnetic contribution arises from the hopping between the two half-filled t_{2g} levels via t_3. While both mechanisms are relevant, the ferromagnetic contributions are typically weaker than antiferromagnetic contributions, so that $J_1 > 0$ (in part, because $|t_3| > \tilde{t}$). For heavier ligands, the increasing $\tilde{t}$ should enhance the ferromagnetic contribution primarily, resulting in a decreased magnitude of J_1.

Finally, for the high-spin d^5 case (i.e., MnX_2), the overall magnitude of the couplings is generally expected to be weak. While both $\tilde{t}$ and t_3 hopping processes contribute with antiferromagnetic contributions due to half-filled t_{2g} and e_g levels, their effects are reduced. This can be understood by considering the energy cost for transfer of an electron between

metal sites is the largest for the case of half filling [45]. This can be understood by considering the effects of Hund's coupling; for a process $(\uparrow\uparrow\uparrow\uparrow\uparrow, \downarrow\downarrow\downarrow\downarrow) \rightarrow (\uparrow\uparrow\uparrow\uparrow, \downarrow\downarrow\downarrow\downarrow\uparrow)$, the total Coulomb repulsion experienced by the electron at its parent site is mitigated by the spin alignment through Hund's coupling. After hopping, the electron's spin is necessarily antialigned with all other electrons, so that the full Coulomb repulsion is felt. For this reason, the cost for electron transfer is large $\sim U + 4J$. This suppresses the antiferromagnetic exchange sufficiently that ferromagnetic exchange processes not captured in the d-only picture are competitive, resulting in an overall suppression of the nearest-neighbor interactions. Full discussion of this situation is provided in the following sections.

C. Anisotropic interactions

In this work, we consider d^3, high-spin d^5, and d^8 filling because the ground states possess no orbital degeneracy, and the orbital angular momentum is quenched at zeroth order. In addition, the atomic spin-orbit coupling for third row metals is relatively weak. For this reason, magnetic anisotropy associated with the metal alone is mostly negligible, allowing the effects of introducing heavy ligands to be investigated in detail. We discuss these effects again in terms of the effective d-only model, where the atomic SOC of the ligands ($\mathcal{H}_{\mathrm{SOC}} = \xi \sum_l \mathbf{L}_l \cdot \mathbf{S}_l$) is downfolded into effective d-d hopping and on-site terms. Such terms can be estimated via Wannier projection techniques applied to fully relativistic DFT calculations, as shown in the following sections. In general, such single-particle contributions then take the form:

$$\mathcal{H}_{\mathrm{hop}} = \sum_{lm} \sum_{\alpha\beta} \underline{c}_{l\alpha}^{\mathrm{T}} \left\{ t_{\alpha\beta}^{lm} \, \mathbb{I} + \frac{i}{2} \left(\vec{\lambda}_{\alpha\beta}^{lm} \cdot \vec{\sigma} \right) \right\} \underline{c}_{m\beta} \qquad (3)$$

in terms of the Pauli matrices σ and electron annihilation operators on site l and orbital α, $\underline{c}_{l\alpha} = (c_{l\alpha\uparrow} \quad c_{l\alpha\downarrow})$ and its transpose $\underline{c}_{l\alpha}^{\mathrm{T}}$. Here, the $t_{\alpha\beta}^{lm}$ represent the regular spin-independent hopping and crystal field terms between orbital α at metal site l and β at site m. The vector $\vec{\lambda}_{\alpha\beta}^{lm}$ then parameterizes the complex spin-dependent terms resulting from spin-orbit coupling. For example, the contribution from the atomic SOC at the metal site M corresponds to $\vec{\lambda}_{\alpha\beta}^{ll} = -i \, \xi_{\mathrm{M}} \langle\alpha|\mathbf{L}|\beta\rangle$. With inclusion of heavy ligands with large SOC constants ξ, there are two main effects.

The first effect is to induce spin-dependent crystal field terms as a result of p-d hybridization that mimic the atomic SOC. For example, the metal d_{xy} orbital may hybridize with the ligand p_y orbital, while the d_{xz} hybridizes with the ligand p_z orbital. The effects of SOC at the ligand is then to make an effective matrix element between the d orbitals via the sequence $d_{xy} \xrightarrow{\mathrm{hop}} p_y \xrightarrow{L_x S_x} p_z \xrightarrow{\mathrm{hop}} d_{xz}$. When downfolded into the d-only picture, this mimics the effects of $L_x S_x$, with an effective SOC constant that scales with the atomic constant of the ligand and the degree of metal-ligand hybridization. However, as discussed further in Appendix C, the matrix elements of the induced SOC are not restricted to take the atomic form. They are the primary source of single-ion anisotropy, but the effects are difficult to anticipate *a priori*. We can anticipate only that the SIA should generally grow for heavier ligands.
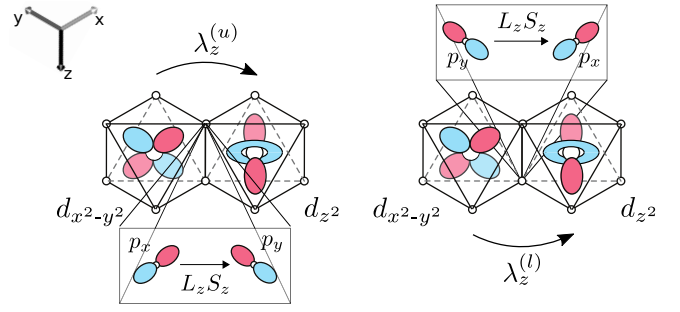

FIG. 3. Illustration of predominant nearest-neighbor spin-dependent hopping λ_z, arising from spin-orbit coupling effects on a Z_1 bond (defined in Fig. 1). It results from the hopping along the upper ($\lambda_z^{(u)}$) and lower ($\lambda_z^{(l)}$) paths: $\lambda_z = \lambda_z^{(u)} + \lambda_z^{(l)}$.

Experimentally, $3d^3$ and $3d^5$ materials tend to have weak SIA, while larger variations are seen for $3d^8$ materials [46].

The second effect concerns complex hopping between sites. The GKA rules can be modified to treat complex hoppings. For bonds with inversion symmetry, contributions at order $t\lambda$ in perturbation theory vanish precisely. Interactions arising at order $(\lambda)^2$ take the form $J_\mu (2S_l^\mu S_m^\mu - \mathbf{S}_l \cdot \mathbf{S}_m)$, where μ refers to the direction of $\vec{\lambda}$. The sign of J_μ is the same as anticipated from the GKA rules. Thus spin-dependent hopping between half-filled orbitals results in an antiferromagnetic Ising term plus a ferromagnetic Heisenberg term of half the magnitude. The converse applies to hopping from half-filled orbitals to filled or empty orbitals. For all edge-sharing materials, the largest nearest-neighbor $\vec{\lambda}_{\alpha\beta}^{lm}$ terms correspond to hopping between the e_g orbitals, which tend to hybridize with the ligands to a much higher degree than the t_{2g} orbitals. As a representative example, there are two relevant sequences for the Z_1 bond: $d_{x^2-y^2} \xrightarrow{\mathrm{hop}} p_x \xrightarrow{L_z S_z} p_y \xrightarrow{\mathrm{hop}} d_{z^2}$ [$\lambda_z^{(u)}$, via the upper path depicted in Fig. 3] and $d_{x^2-y^2} \xrightarrow{\mathrm{hop}} p_y \xrightarrow{L_z S_z} p_x \xrightarrow{\mathrm{hop}} d_{z^2}$ ($\lambda_z^{(l)}$, via the lower path). Due to the specific phases of the orbitals, these paths add constructively, $\lambda^z = \lambda_z^{(u)} + \lambda_z^{(l)}$. Within the spin-dependent hopping picture, this manifests into a particularly large $\lambda_{(x^2-y^2,z^2)}^z$. As discussed previously in Ref. [31], this may be associated with an antiferromagnetic Kitaev coupling for d^8 filling.

More generally, we expect strong bilinear anisotropic terms in materials with half-filled e_g orbitals, provided the ligands are sufficiently heavy. This applies most readily to d^8 filling, since materials with d^5 filling have reduced p-d hybridization. In contrast, the d^3 materials, with empty e_g orbitals, are expected to exhibit much weaker anisotropic exchange. The above trends and mechanisms highlight that electron filling and bonding geometry play crucial roles in the relative anisotropy of the magnetic couplings.

IV. MAGNETIC EXCHANGE COUPLINGS FOR MONOLAYER MX_2

In this section, we present estimates for the magnetic exchange couplings in monolayer MX_2 by employing the *ab initio* based projED and four-state methods, and discuss results with the expected trends introduced above. The four-state method is based on total energy mapping through

noncollinear, magnetic DFT calculations, including SOC. Each magnetic interaction parameter is related to the energies of four distinct magnetic configurations [33,34]. The projED method consists of two steps: (i) a finite-cluster Hubbard Hamiltonian is constructed based on Wannier projection of a nonmagnetic, relativistic band structure calculation; and (ii) the Hubbard Hamiltonian is solved via exact diagonalization (ED) and the corresponding effective spin Hamiltonian is extracted through projection onto the low-energy subspace [32]. In the results below, we employ a d-only basis for projED; as such, the effects of p-d hybridization are downfolded into effective d-only single-particle terms and renormalized Coulomb terms discussed in Sec. III A. While this allows to capture the majority of contributions to the magnetic exchange, as recently pointed out for the d^7 case [47], there is one important contribution omitted, which represents the regular ferromagnetic Goodenough-Kanamori exchange for 90° bonds. This consists of processes where a hole from each metal site meets on a single ligand in different orbitals, and interact via Hund's coupling. Perturbative corrections due to this process are mentioned in each section. Further descriptions of both methods and their relative merits are provided in Appendix B.

In Appendix E, we list results obtained with alternative U_{avg} and J_{avg} values for all nine investigated materials with both methods. These values were previously used by some of the authors in other works on the NiX_2 materials [27,48]. The comparison to the results below highlights the independence of the qualitative trends obtained by the two employed methods on these input parameters.

A. d^8 $S = 1$ materials NiX_2

Experimentally, all bulk NiX_2 materials exhibit magnetic long-range order and were subject of intense investigation a few decades ago due to their metamagnetic and multiferroic behavior [23,24,49,50]. For the monolayer structures, previous theoretical analysis by some of the authors indicated a range of possible ground states: from a topological spin lattice [48], composed of vortices and antibivortices to other competing commensurate and incommensurate phases [48,51,52], including a multiferroic spin spiral state [27].

In Table II, we report the exchange parameters of model Eq. (1) as defined in Eq. (2) for NiX_2 monolayers. Values are computed using the projED and four-state methods, employing U_{avg} and J_{avg} values estimated via the cRPA approach (Table I).

In agreement with the expectations addressed in Sec. III, we find J_1 to be ferromagnetic (i.e., $J_1 < 0$) and increasing across the series Cl-Br-I due to increased metal-ligand hybridization. In d^8 materials, with half-filled e_g orbitals, exchange processes with multiple holes on a single ligand lead to significant ferromagnetic corrections to the value of J_1 obtained with projED. As detailed in Appendix B, we estimate with perturbation theory $\delta J_1 \sim -2$ to -5 meV. It should therefore be noted that the ferromagnetic ligand-mediated exchange δJ_1 is for d^8 filling the largest contribution to J_1. This can be expected because the e_g orbitals hybridize strongly with the p orbitals. The signs and overall magnitudes obtained

TABLE II. Exchange parameters (in meV) for the NiX_2 monolayer structures using the respective (U_{avg}, J_{avg}) parameters determined with cRPA for each material (see Table I); extracted with the projED method (left) and the four-state energy mapping method (right). Note that for the projED method J_1 should be corrected with $\delta J_1 \sim -2$ to -5 meV to take additional ferromagnetic contributions into account (see Appendix B).

NiX_2	projED			four-state		
	NiCl$_2$	NiBr$_2$	NiI$_2$	NiCl$_2$	NiBr$_2$	NiI$_2$
J_1	−0.7	−0.8	−1.2	−2.9	−3.9	−6.2
K_1	0.0	+0.1	+1.0	0.0	+0.2	+2.2
Γ_1	0.0	0.0	0.0	0.0	0.0	0.0
Γ_1'	0.0	0.0	−0.1	0.0	0.0	−0.1
J_2	0.0	0.0	0.0	−0.1	−0.1	−0.2
J_3	+0.6	+1.0	+1.8	+0.8	+1.8	+4.2
A_c	0.0	+0.1	+0.8	0.0	0.0	+0.4

for the monolayers are compatible with the bulk values; for example, bulk NiCl$_2$ orders ferromagnetically in plane [49,53,54], with ESR and neutron scattering experiments estimating $J_{1,bulk} \approx -3.6$ meV.

In both theoretical approaches, we find that the nearest-neighbor anisotropic exchange is well represented by an antiferromagnetic Kitaev term K_1, which may be quite substantial compared to J_1 in NiBr$_2$ and NiI$_2$. The magnitude of K_1 scales with the SOC strength of the ligand, clearly identifying the origin of the interaction as the hopping process depicted in Fig. 3. These findings are compatible with previous work on superexchange processes mediated by p-orbital anions with strong SOC [31], such as the $S = 1$ NiI$_2$ or the $S = 3/2$ Cr^{3+} monolayer systems [15,55]. For example, Ref. [31] anticipated significant AFM Kitaev interactions in d^8 compounds. In that case, a subset of exchange processes were considered, leading to the prediction $K_1 \gtrsim 2|J_1|$. Here, we find that the previously omitted correction δJ_1 somewhat reduces this ratio, but relatively large AFM Kitaev interactions still seem to be realised in NiI$_2$.

For the longer range couplings, a vanishingly small J_2 and significant antiferromagnetic J_3, i.e. $|J_1| > |J_3| \gg |J_2|$, is found in both methods. These results can again be understood by considering the dominant hoppings. For the second and third nearest neighbors, we discuss the Z_2 and Z_3 bonds, defined in Fig. 1(a). The hoppings between sites on a Z_2 bond are dominated by $\tilde{t} = t_{(xy,z^2)}$ and $t_2 = t_{(xz,yz)}$. For the Z_3 bond, we find $t_3 = t_{(xy,xy)}$, $t_5 = t_{(x^2-y^2,x^2-y^2)}$, and $t_6 = t_{(z^2,z^2)}$ to be the largest. For second neighbors, the d^8 filling ensures that only the t_{2g}-e_g hopping $\tilde{t}$ is relevant, which leads to a weak ferromagnetic interaction. This contribution is expected to be smaller than the nearest-neighbor coupling by a factor $\sim(t_{2nn}/t_{nn})^2$, which explains the relative suppression. In contrast, for third neighbors, there are large e_g-e_g hoppings that arise from ligand-assisted hopping paths such as $d_{x^2-y^2} \xrightarrow{\text{hop}} p_x \xrightarrow{\text{hop}} p_y \xrightarrow{\text{hop}} d_{x^2-y^2}$ that are enhanced by metal-ligand hybridization and the spatial extent of the ligand p orbitals. This results in large third neighbor t_5 and t_6, producing significant third neighbor antiferromagnetic couplings, which tend to increase in magnitude across the series Cl-Br-I. In fact, with

both projED and four-state approaches, we find that $J_3/|J_1|$ increases toward a significant contribution across this series.

Regarding the single-ion anisotropy A_c, with both projED and four-state methods, we generally find $A_c > 0$, with a magnitude that increases with the SOC strength of the ligand. This is compatible with bulk trends. For bulk $NiCl_2$, the single-ion anisotropy was determined to be finite, but small, i.e., below 0.01 meV [49,54]. For bulk $NiBr_2$, SIA was experimentally [56] estimated to be larger $A_c \sim 0.08 \pm 0.05$ meV, which is similar to the monolayer projED estimation $A_c \approx 0.1$ meV. While it is tempting to attribute this effect to an increase in the effective SOC of the metal via d-p hybridization, the situation is not so simple, as outlined in Appendix C.

The classical ground states of the triangular Heisenberg model with isotropic ferromagnetic J_1 and competing FM or AFM J_2, J_3 have been thoroughly investigated in the past [57]. Our estimated range of parameters are compatible with two possible magnetic ground states for NiX_2 monolayers, namely a ferromagnetic or an incommensurate helix with ordering wave vector $q_{2D} = (q, q)$, the latter displaying lower energy when $4J_3 \gtrsim |J_1| + 3|J_2|$. The increasing trend of $J_3/|J_1|$ across the Cl-Br-I series indicates an enhanced tendency to stabilise incommensurate helimagnetism for heavier ligands, with $NiCl_2$ monolayer being very close to the FM-spiral phase boundary. These trends can be compared to their bulk counterparts, keeping in mind that interlayer interactions may also affect the magnetic properties of the latter.

Bulk $NiCl_2$ orders ferromagnetically in the plane [49,53,54] with an ordering wavevector $q_{3D} = (0, 0, 1.5)$ signaling AFM interlayer interaction between the planes. On the other hand, $NiBr_2$ and NiI_2 undergo a series of transitions: upon decreasing temperature, they both enter first a similar state to bulk $NiCl_2$ of antiferromagnetically coupled ferromagnetic sheets [50,58–62], but then upon decreasing T further, they enter another, incommensurate spiral phase [56,58–65]. For $NiBr_2$, the spiral displays a wave vector $(q, q, 1.5)$ with small $q \sim 0.03$ and spins lying in the plane of the layer [56,59]. Such a phase can be understood in the context of a model with ferromagnetic J_1, antiferromagnetic J_3, and $A_c > 0$ with $J_3/|J_1| \gtrsim 0.25$ [57], as well as antiferromagnetic interlayer exchange [56], thus demonstrating a significant $J_3 > 0$ in the bulk materials. These parameter trends are fully consistent with our monolayer calculations.

For bulk NiI_2, the spiral develops concomitantly with a structural transition from rhombohedral to monoclinic cell and displays instead a wave vector $(q, 0, \sim 1.46)$, with $q \gtrsim 0.1$ and moments oriented in the plane perpendicular to one of the cubic axes ($\sim 35°$ from the plane) [62]. Such an orientation is difficult to understand without invoking bond-dependent couplings referenced to the cubic axes. Since the ordering vector is perpendicular to a bond, the ordering pattern consists of stripes in which moments linked by one of the nearest-neighbor bond types are always aligned in parallel. In the presence of a sizable antiferromagnetic $K_1 > 0$, there is an energetic preference for the moments to align in the plane perpendicular to the associated cubic axis of the bond perpendicular to the q vector. This is precisely what is observed experimentally. Thus the particular moment orientation should be taken as evidence for significant $K_1 > 0$ in bulk NiI_2. Albeit the larger ordering wave vector of bulk NiI_2 is

TABLE III. Exchange parameters (in meV) for the VX_2 monolayer structures using the respective (U_{avg}, J_{avg}) parameters determined with cRPA for each material (see Table I); extracted with the projED method (left) and the four-state energy mapping method (right).

VX_2	projED			four-state		
	VCl_2	VBr_2	VI_2	VCl_2	VBr_2	VI_2
J_1	+4.9	+3.6	+2.6	+4.2	+2.5	+0.6
K_1	0.0	0.0	0.0	0.0	0.0	−0.1
Γ_1	0.0	0.0	0.0	0.0	0.0	+0.1
Γ_1'	0.0	0.0	0.0	0.0	0.0	0.0
J_2	0.0	+0.1	+0.1	0.0	0.0	+0.1
J_3	0.0	+0.1	+0.1	0.0	+0.1	+0.2
A_c	0.0	0.0	0.0	0.0	0.0	0.0

still consistent with our prediction of increasing magnetic frustration across the Cl-Br-I series, the in-plane component of bulk q_{3D} would suggest, within an isotropic Heisenberg model, a strong antiferromagnetic J_2 [57,62]. Such a significant deviation from expected and estimated trends for magnetic interactions in the NiX_2 class is difficult to rationalize, and one may wonder how appropriate it is to compare bulk and monolayer NiI_2. A recent experimental analysis of NiI_2 magnetic properties down to the monolayer limit via complementary optical techniques could not resolve the 2D ordering wave vector, both $q_{2D} = (q, q)$ and $(q, 0)$ being compatible with the detected symmetries [27]. At the same time, a quite strong AFM interlayer interaction, $\sim 0.45|J_1|$, was deduced from the layer-dependent spiral transition temperature [27], much larger than the interlayer exchange of $NiBr_2$, $\sim 0.1|J_1|$ [56]. These facts suggest that other mechanisms, not included in the 2D model considered here, may play an important role in shaping the bulk magnetic properties of NiI_2.

Finally, we note that a large nearest-neighbor biquadratic exchange $B(\mathbf{S}_i \cdot \mathbf{S}_j)^2$ with $B < 0$ was recently invoked to explain the collinear ground state of $NiCl_2$, compared to noncollinear helimagnetic ground states of $NiBr_2$ and NiI_2 [51]. To test the possibility of large B, we also computed all higher order couplings using projED for the monolayer structure, which is capable of capturing four-spin interactions [66]. However, we find no four-spin terms exceeding 0.01 meV. This result can be understood from the fact that B arises at order t^4/U^3 in perturbation theory, and is generally expected to be significant for nearly itinerant electrons. Nonetheless, it could still be relevant for systems like $NiCl_2$ that are at the verge of the FM-spiral phase transition and, as such, sensitive to other weak interactions not included in the model Eq. (1).

B. d^3 $S = 3/2$ materials VX_2

For VX_2 compounds, the exchange parameters extracted with both *ab-initio* methods are given in Table III. Good agreement is found both in magnitude and trends between four-state and projED approaches.

We find antiferromagnetic nearest-neighbor Heisenberg coupling J_1, with a decreasing magnitude as a function of the ligand atomic number. As outlined in Sec. III,

the dominant hopping processes suggest a competition between antiferromagnetic and ferromagnetic contributions in VX_2, resulting in a net antiferromagnetic interaction; the ligand-assisted hoppings become more important for the heavier ligands, leading to a stronger contribution of the ferromagnetic exchange and resulting in the overall decrease of $|J_1|$ across the series Cl-Br-I.

The second and third nearest-neighbor couplings, J_2 and J_3, respectively, turn out to be small generally. This can be understood considering the primary third neighbor hopping occurs between e_g orbitals via paths like $e_g \xrightarrow{\text{hop}} p \xrightarrow{\text{hop}} p \xrightarrow{\text{hop}} e_g$. For d^3 filling, such hoppings are irrelevant to the magnetic couplings. As a result, the long-range interactions are suppressed compared to d^8 filling. Similarly, consistent with the discussion in Sec. III, the bilinear anisotropic exchange is negligible, since the ligand SOC only makes relevant corrections to hopping between e_g orbitals.

Our results show consistency with behaviors experimentally observed in the VX_2 bulk systems. Estimated intralayer nearest-neighbor exchange couplings fitting data from susceptibility [67] and INS data [68,69], were reported to be $J_1 = +3.8$ meV and $J_1 = +2.8$ meV, for bulk VCl_2 and VBr_2, which supports the *ab initio* trends. Moreover, the AFM Néel 120° spin order was observed, with transition temperatures of $T_N = 36$ and 29 K, for the two systems respectively [68–71]. In accordance with our *ab initio* intralayer estimates, these results suggest that monolayer VCl_2 and VBr_2 can be sufficiently described by short-range AFM interactions. Given the absence of anisotropic couplings, we would expect these ordering temperatures to be significantly reduced in monolayers. However the ordering pattern is not expected to differ.

At variance, the physics of VI_2 appears less obvious. Bulk VI_2 displays AFM 120° correlations at high temperature, but ultimately orders at $T_{N_2} = 14.4$ K into an AFM collinear zigzag stripe order [70,72]. No experimental estimates of J_1 are available (to the best of our knowledge). However, the lower T_N values with respect to VCl_2 and VBr_2 suggest reliability of our *ab initio* estimates: the former suggests energetic competition between AFM phases that could be ascribed to the nonzero intralayer J_3 contribution estimated in monolayer VI_2; the latter supports the argued J_1 decrease across the series Cl-Br-I (Table III).

C. d^5 $S = 5/2$ materials MnX_2

As discussed in Sec. III, the magnetic exchange interactions in MnX_2 are expected to be relatively suppressed as a consequence of the large energy cost for transfer of electrons between metal sites. This is indeed what is found with both projED and four-state approaches, as detailed in Table IV. Due to the partially filled e_g orbitals, J_1 obtained with projED has to be corrected, with $\delta J_1 \sim -0.4$ to -0.9 meV (see Appendix B). The nearest-neighbor Heisenberg J_1 exchange is found to be antiferromagnetic, with little variation with ligand elements, in contrast to the behaviors discussed for NiX_2 and VX_2. Anisotropic exchange associated with the $e_g \xrightarrow{\text{hop}} p \xrightarrow{\text{hop}} p \xrightarrow{\text{hop}} e_g$ hopping processes should be finite, but it represents only a small fraction of the total contributions, and is therefore negligible. With both approaches we find longer range couplings J_2 and J_3 in the range 0.01 to

TABLE IV. Exchange parameters (in meV) for the MnX_2 monolayer structures using the respective $(U_{\text{avg}}, J_{\text{avg}})$ parameters determined with cRPA for each material (see Table I); extracted with the projED method (left) and the four-state energy mapping method (right). Note that for the projED method J_1 should be corrected with $\delta J_1 \sim -0.4$ to -0.9 meV to take additional ferromagnetic contributions into account (see Appendix B).

| MnX_2 | projED | | | four-state | | |
	$MnCl_2$	$MnBr_2$	MnI_2	$MnCl_2$	$MnBr_2$	MnI_2
J_1	+0.8	+0.7	+0.7	+0.1	+0.1	+0.1
K_1	0.0	0.0	0.0	0.0	0.0	0.0
Γ_1	0.0	0.0	0.0	0.0	0.0	0.0
Γ_1'	0.0	0.0	0.0	0.0	0.0	0.0
J_2	0.0	0.0	0.0	0.0	0.0	0.0
J_3	0.0	+0.1	+0.1	0.0	0.0	+0.1
A_c	0.0	0.0	0.0	0.0	0.0	0.0

0.1 meV, which may be significant given the relative suppression of J_1.

Consistently with the nearly suppressed magnetic exchange interactions, very low experimental transition temperatures are reported for the bulk MnX_2 systems. Particularly, bulk $MnCl_2$ and $MnBr_2$ exhibit two successive transitions at $T_{N_1} = 1.96$ K, $T_{N_2} = 1.81$ K [73] and $T_{N_1} = 2.32$ K, $T_{N_2} = 2.17$ K [74–76] respectively. In both cases, the intermediate phase has been identified as an incommensurate phase, and the low-temperature structure as a double stripe order phase. Bulk MnI_2 exhibits even three subsequent magnetic transitions below 4 K [74,76]. The lowest temperature phase was identified as a spiral order with an incommensurate wave vector [77]. Given the very small magnitude of the exchange couplings and large $S = 5/2$, we agree with previous speculations [76,78] that long-range dipolar interactions may ultimately be relevant for both, bulk and monolayer systems.

V. CONCLUSIONS

With this study we investigated the effective magnetic models in the monolayer family of triangular lattice materials MX_2 ($M=$V, Mn, Ni and $X=$Cl, Br, I), where spin-orbit coupling effects are dominantly caused by the ligand element. We also took the opportunity of such a larger study to benchmark two *ab initio* methods used to extract effective spin models for real materials.

Considering the very different nature of the two *ab initio* based methods considered here, the results agree remarkably well in terms of signs and trends in the relative magnitudes. The points of disagreement are typically the overall magnitude. Among others, this may be assigned to the implementation of the parameter values U_{avg} and J_{avg}, since they enter either in the Hubbard Hamiltonian for projED, or in the DFT + U framework for the four-state method. For consistency, we compared both methods using the same parameter values in spite of the fact that this may not be the ideal parameter set especially for the four-state method. On the other hand, in the four-state method an overall linear dependence varying these parameters was found (compare Table IX) while the projED

method relies stronger on choosing appropriate parameter sets such as the ones used in this work, obtained with cRPA. In the case of half-filled e_g orbitals for the projED method, ferromagnetic contributions from additional processes have to be considered, which we estimated here via perturbation theory.

Regarding the magnetic parameters for the triangular lattice compounds in general, we find trends for the monolayer structures consistent with expectations based on experimental observations in the bulk case. Noticeably, for monolayer NiI_2 we do find sizable Kitaev coupling suggested in previous works [31,48], as well as large ferromagnetic J_1 and significant antiferromagnetic J_3 isotropic couplings. The VX_2 monolayer structures can all be described well in the framework of nearest-neighbor AFM Heisenberg models, and the MnX_2 materials reveal overall suppressed magnetic exchange, hinting at long-range dipolar interactions as potentially the most important factor for the magnetic ground state.

Finally, already the use of simplified models made it possible to understand the underlying mechanism of the magnetic exchange in the triangular MX_2 compounds. Consideration of two dominant hopping parameters enabled us to identify the (anti)ferromagnetic nature of J_1 in the (d^3) d^8 materials, including the trends of additional or competing ferromagnetic contributions for larger ligands. Our analysis further allows for a physical insight in the peculiar situation of d^8 materials, displaying (i) significant enhancement of the third nearest-neighbor exchange interaction J_3, especially when compared to shorter-range J_2, and (ii) substantial anisotropic exchange/Kitaev interactions, increasing with ligand atomic number. The first effect can be understood only if the specific hopping interactions and involved orbital states contributing to the exchange interactions are properly taken into account: as the hopping processes relevant for J_2 and J_3 are fundamentally different, the conventional expectation that exchange interaction should roughly scale with the inverse of the bond length is, at best, inaccurate. Additionally, J_3 is dominated by ligand-assisted hopping processes, and as such can be directly tuned by the metal-ligand hybridization (hence by appropriate choices of the ligand). Similarly, relativistic anisotropic exchanges arise mostly from ligands spin-orbit coupling, which tunes through ligand-assisted hoppings the effective SOC between the magnetic ions and strongly modifies its matrix elements as compared to the atomic limit. It follows that the resulting strength of the anisotropic exchange found in d^8 materials is mostly driven by the atomic SOC of the ligands, as well as by the metal-ligand hybridization again. The emerging picture thus possibly suggests strategies to enforce magnetic frustration and Kitaev-type interactions, both sought for in the quest of exotic magnetic phases, alternative to existing ones based mostly on suitable choices of heavier ($4d$ or $5d$) transition metals.

APPENDIX A: RELATION BETWEEN EXCHANGE VALUES IN CRYSTALLOGRAPHIC AND CUBIC COORDINATE SYSTEMS

The parametrization convention used in the main text follows the extended Heisenberg-Kitaev model with focus on the bond-dependent Ising-like Kitaev interaction. With this convention it is easy to identify such general bond-dependent parameters. For example, on a Z_1 bond between sites l and m, the magnetic exchange matrix is defined as follows:

$$\mathbb{J}_{lm}^{Z_1} = \begin{pmatrix} J & \Gamma & \Gamma' \\ \Gamma & J & \Gamma' \\ \Gamma' & \Gamma' & J + K \end{pmatrix}, \tag{A1}$$

while on an X_1 bond it can be determined by C_3 rotation about the out-of-plane axis arriving at

$$\mathbb{J}_{lm}^{X_1} = \begin{pmatrix} J + K & \Gamma' & \Gamma' \\ \Gamma' & J & \Gamma \\ \Gamma' & \Gamma & J \end{pmatrix}. \tag{A2}$$

Alternatively, the interactions can also be expressed in a coordinate system oriented along the crystal axes (ab^*c), where b^* is perpendicular to a and c. By symmetry, the magnetic exchange on a bond along the a axis (e.g., Z_1 bond) can be parametrized with

$$\mathbb{J}_{lm}^{Z_1} = \begin{pmatrix} J_{aa} & 0 & 0 \\ 0 & J_{b^*b^*} & J_{b^*c} \\ 0 & J_{b^*c} & J_{cc} \end{pmatrix}. \tag{A3}$$

The corresponding exchange matrix on the X_1 bond can then be again obtained by C_3 rotation about the c axis:

$$\mathbb{J}_{lm}^{X_1} = \begin{pmatrix} \frac{1}{4}(J_{aa} + 3J_{b^*b^*}) & -\frac{\sqrt{3}}{4}(J_{aa} - J_{b^*b^*}) & -\frac{\sqrt{3}}{2}J_{b^*c} \\ -\frac{\sqrt{3}}{4}(J_{aa} - J_{b^*b^*}) & \frac{1}{4}(3J_{aa} + J_{b^*b^*}) & -\frac{1}{2}J_{b^*c} \\ -\frac{\sqrt{3}}{2}J_{b^*c} & -\frac{1}{2}J_{b^*c} & J_{cc} \end{pmatrix}. \tag{A4}$$

Both approaches are equivalent and can be directly translated into each other via the following relations:

$$J = \frac{1}{6}(3J_{aa} + J_{b^*b^*} + 2J_{cc} + 2\sqrt{2}J_{b^*c}), \tag{A5}$$

$$K = \frac{1}{2}(-J_{aa} + J_{b^*b^*} - 2\sqrt{2}J_{b^*c}), \tag{A6}$$

$$\Gamma = \frac{1}{6}(-3J_{aa} + J_{b^*b^*} + 2J_{cc} + 2\sqrt{2}J_{b^*c}), \tag{A7}$$

$$\Gamma' = \frac{1}{6}(-2J_{b^*b^*} + 2J_{cc} - \sqrt{2}J_{b^*c}). \tag{A8}$$

TABLE V. Obtained structural parameters from DFT-calculations for the studied triangular MX_2 monolayer systems. In order of appearance: in-plane lattice parameters $|a|$ (* labels experimental data for bulk structures reported in Ref. [80]); M-X and X-X bond lengths; M-$\hat{X}$-M bond angles. Due to the trigonal distortion, shorter and longer X-X bonds are reported with associated bond angles.

	$|a|$ (Å)	M-X (Å)	X-X (Å)	M-$\hat{X}$-M
NiCl$_2$	3.48* 3.49	2.40	3.30–3.49	86.73°–93.27°
NiBr$_2$	3.7* 3.69	2.55	3.52–3.69	87.26°–92.74°
NiI$_2$	3.9* 3.96	2.74	3.78–3.96	87.33°–92.67°
VCl$_2$	3.6* 3.54	2.48	3.47–3.54	88.93°–91.07°
VBr$_2$	3.77* 3.75	2.64	3.71–3.75	89.36°–90.64°
VI$_2$	4.06* 4.05	2.84	3.99–4.05	89.11°–90.89°
MnCl$_2$	3.71* 3.70	2.55	3.50–3.70	86.84°–93.16°
MnBr$_2$	3.89* 3.88	2.70	3.76–3.88	88.13°–91.87°
MnI$_2$	4.15* 4.15	2.91	4.07–4.15	88.91°–91.09°

Independent of the coordinate system, the exchange matrix can conventionally be decomposed into three distinct contributions. The fully isotropic part with respect to spin orientations——in contrast to bond anisotropy—corresponds to $J_{lm}^{\text{iso}} = \frac{1}{3}\text{Tr}(\mathbb{J}_{lm})$. In the case of the cubic coordinate system with Eq. (A1), this would correspond to $J_{lm}^{\text{iso}} = J + K/3$. The anisotropic terms with respect to spin orientation are composed of the symmetric term, $\mathbb{J}_{lm}^{\text{S}} = \frac{1}{2}(\mathbb{J}_{lm} + \mathbb{J}_{ml}) - J_{lm}^{\text{iso}}\mathbb{I}$ and the anti-symmetric term $\mathbb{J}_{lm}^{\text{A}} = \frac{1}{2}(\mathbb{J}_{lm} - \mathbb{J}_{ml})$. The latter vanishes in the presence of an inversion center in the middle of the bond, as it is the case for the materials investigated in this work.

APPENDIX B: METHODS

1. Monolayer MX_2 structures

Within the projED and four-state methods, calculations have been performed on fixed triangular MX_2 monolayer structures, which have been fully relaxed through structural relaxations as implemented in VASP [79], within the generalized gradient approximation (GGA) and Perdew-Burke-Erzenhof (PBE) [39] functional. Particularly, no Hubbard-U and SOC corrections were employed for all the structures' optimization, whereas different magnetic orderings were considered according to calculated energetics (i.e., lowest energy configuration without SOC contribution): FM order for NiX_2 systems, consistent with previous works [48] and 120° AFM order for MnX_2 and VX_2 systems. The plane wave cutoff energy was set to 600 eV for NiCl$_2$ and NiBr$_2$, and to 500 eV for the other MX_2 systems. The sampling of the Brillouin zone for the monolayer unit cell relied on a Γ-centered $18 \times 18 \times 1$ **k**-point mesh, and meshes for the supercells have been scaled accordingly. The Gaussian-smearing method, with a broadening (SIGMA) smaller than 0.05 eV, was used to determine the bands' occupation. The obtained in-plane lattice parameters ($|a| = |b|$) and other structural parameters of interest are reported in Table V; the **c** length was fixed to 20.8 Å, to insert a vacuum distance between periodic repetition of the layers along this direction.

2. Constrained RPA

We estimated the electronic two-particle interaction terms with the constrained random-phase approximation [40,41], as implemented in the FHI-gap code [81]. The approach is similar to a recent cRPA study [82], applied here for the discussed relaxed monolayer structures and considering the full five 3d orbitals of the metal elements in each case. The atomic-like spherical symmetric expressions for d block electrons derived from Slater integrals [83] F_k can be obtained via the following relations (for orbitals α, β and angular momentum quantum number l):

$$U_{\text{avg}} = \frac{1}{(2l+1)^2}\sum_{\alpha\beta}U_{\alpha\beta} = F_0, \tag{B1}$$

$$J_{\text{avg}} = \frac{7}{5}\frac{1}{2l(2l+1)}\sum_{\alpha\neq\beta}J_{\alpha\beta} = \frac{F_2 + F_4}{14}. \tag{B2}$$

3. ProjED

The projED method [32] consists of two main steps. First, an effective electronic multi-orbital Hubbard Hamiltonian $\mathcal{H}_{\text{tot}}$ is determined:

$$\mathcal{H}_{\text{tot}} = \mathcal{H}_{\text{hop}} + \mathcal{H}_{\text{U}}, \tag{B3}$$

$$\mathcal{H}_{\text{hop}} = \sum_{lm\alpha\beta}\sum_{\sigma\sigma'}t_{l\alpha,m\beta}^{\sigma\sigma'}c_{l\alpha\sigma}^{\dagger}c_{m\beta\sigma'}, \tag{B4}$$

$$\mathcal{H}_{\text{U}} = \sum_{l\,\alpha\beta\gamma\delta}\sum_{\sigma\sigma'}U_{l\alpha\beta\gamma\delta}^{\sigma\sigma'}c_{l\alpha\sigma}^{\dagger}c_{l\beta\sigma'}^{\dagger}c_{l\delta\sigma'}c_{l\gamma\sigma}, \tag{B5}$$

where $\{l, m\}$ are site, $\{\alpha, \beta, \gamma, \delta\}$ orbital, and $\{\sigma, \sigma'\}$ spin indices. $\mathcal{H}_{\text{hop}}$ describes nonmagnetic hopping processes between the 3d electronic (spin-)orbitals of the transition metals $M =$ Ni, V, Mn and $\mathcal{H}_{\text{U}}$ the respective two-particle Coulomb interaction. The hopping parameters were computed *ab initio* using the Full Potential Local Orbital [44] (FPLO) code within the generalized gradient approximation [39] (GGA) for each monolayer structure. The hopping parameters are extracted via Wannier projection based on full relativistic non-spin-polarized band structures. All calculations were performed with a $12 \times 12 \times 12$ **k**-point mesh and the tetrahedron method was employed for the Brillouin zone integration.

Hopping parameters based on relativistic DFT calculations allow to effectively consider the influence of the heavy ligands involved, especially in the case of the MI$_2$ series, and results in *complex* hopping parameters. To ensure consistent treatment of the two-particle Coulomb interaction within the investigated series, the Coulomb parameters were extracted for each material within the cRPA method, as described above.

In a second step, an effective spin Hamiltonian is extracted:

$$\mathcal{H}_{\text{eff}} = \mathbb{P}\mathcal{H}_{\text{tot}}\mathbb{P} = \sum_{l\mu m\nu}J_{lm}^{\mu\nu}S_l^{\mu}S_m^{\nu} \tag{B6}$$

with $\mu, \nu \in \{x, y, z\}$. The projection operator $\mathbb{P}$ projects the electronic Hamiltonian onto its low-energy subspace and then maps onto the respective spin operator representation. The low-energy eigenstates, required for the first step, are computed via exact diagonalization of the five-orbital electronic Hamiltonian on finite two-site clusters. After reducing the Hilbert space onto an energetic regime where spin degrees of

freedom are sufficient to describe the relevant physical properties, the Hamiltonian can be mapped from the electronic onto the spin picture using Stevens operators. In case of $S = 1/2$, this would correspond to the well-known Pauli matrices.

Estimating exchange parameters in the above introduced d-only basis, ferromagnetic corrections arising from exchange processes with multiple holes on a single ligand are omitted. These contributions are dominantly relevant for the isotropic interaction in materials with partially filled e_g orbitals, since p orbitals hybridize predominantly with e_g orbitals. We estimate δJ_1 for the relevant fillings via perturbation theory.

For d^8 filling, the ferromagnetic correction to the projED results can then be estimated by

$$\delta J_1 = -\frac{1}{S^2} \frac{\left(t_{pd}^\sigma\right)^4 J_H^p}{\Delta_{pd}^2 (\Delta_{pd} + U_p/2)^2}, \tag{B7}$$

where Δ_{pd} is the charge transfer energy from d to p orbitals, U_p is the excess ligand Coulomb repulsion, J_H^p is the ligand Hund's coupling, and t_{pd}^σ is the e_g-p hopping integral in the Slater-Koster scheme. On the basis of nonrelativistic band-structure calculations, we estimate $t_{pd}^\sigma \sim 1$ eV and $\Delta_{pd} \sim 3$ to 4 eV for NiX_2, while we take $U_p \sim 4$ eV, $J_H^p \sim 0.3\,U_p$ following Ref. [84].

For d^3 filling, the ferromagnetic correction can be approximated by

$$\delta J_1 = -\frac{3}{S^2} \frac{\left(t_{pd}^\pi\right)^4 J_H^p}{\Delta_{pd}^2 (\Delta_{pd} + U_p/2)^2}, \tag{B8}$$

where we estimate the t_{2g}-p hopping $t_{pd}^\pi \sim 0.7$ eV, and $\Delta_{pd} \sim 4$ to 5 eV. Again, we may take $U_p \sim 4$ eV, $J_H^p \sim 0.3\,U_p$ following Ref. [84]. This provides an estimate of $\delta J_1 \sim -0.3$ to -0.7 meV. The correction is significantly reduced compared to the NiX_2 compounds due to the weaker t_{2g}-p hybridization. As a result, the couplings are well approximated by the d-only terms.

For d^5 filling, δJ_1 may be estimated via

$$\delta J_1 = -\frac{1}{S^2} \frac{\left[\left(t_{pd}^\sigma\right)^4 + 2\left(t_{pd}^\sigma\right)^2\left(t_{pd}^\pi\right)^2 + 3\left(t_{pd}^\pi\right)^4\right] J_H^p}{\Delta_{pd}^2 (\Delta_{pd} + U_p/2)^2}. \tag{B9}$$

Taking $t_{pd}^\sigma \sim 1$ eV, $t_{pd}^\pi \sim 0.7$ eV, $\Delta_{pd} \sim 4$ to 5 eV, $U_p \sim 4$ eV, and $J_H^p \sim 0.3\,U_p$ [84] yields an estimate of the correction to $\delta J_1 \sim -0.4$ to -0.9 meV.

Extracting the local single-ion anisotropy, we considered a linked-cluster expansion including two-site clusters in order to take contributions from nearest-neighbor interactions next to the local contributions into account.

For further neighbor interactions, two-site clusters are used with hopping parameters between the relevant sites. Note that this procedure neglects contributions through indirect hopping paths that involve more than two magnetic sites, but is unavoidable for fillings approaching half-filling due to the computationally demanding exact diagonalization step. Especially for long-range interactions such as J_3 this approximation may be cautiously examined. For the NiX_2 series we tested the neglected contributions via linked cluster expansion, as used previously with projED [85], including up to

three magnetic sites. At least for this class of materials we find only minor modifications below 1%.

4. Four-state total energies

The estimate of the magnetic interaction parameters employing the "four-state method" relies on DFT calculations of the total energies associated to various spin configurations to be mapped on the classical spin Hamiltonian written in Eq. (1). This approach is known as energy-mapping analysis. Specifically, the four-state energy mapping method, which is explained in detail in Refs. [15,33], allows us to extract the magnetic exchange interaction, both the isotropic and anisotropic contributions, between a selected pair of magnetic sites by performing DFT plus SOC energy calculations on four ordered noncollinear spin states. It is based on the use of supercells, which allow to exclude couplings with unwanted distant neighbors. The method is however tied to the choice of DFT basis, implementation of exchange correlation functional used in DFT and to specific computational parameters (i.e., k-point sampling, Hubbard U corrections within DFT $+ U$, etc.).

In this work, we performed calculations of the SIA, first and second neighbors interaction using a $5 \times 4 \times 1$ supercell, while a $6 \times 3 \times 1$ supercell was used for the estimate of the third neighbor interaction. Such large cells should exclude a significant influence from next neighbors. We built supercells from the periodic repetition of the MX_2 monolayer unit cell; structural details are reported in Sec. IV.

By means of this method we can obtain all the elements of the exchange tensor for a chosen magnetic pair, thus gaining direct access to the symmetric anisotropic exchange part (or two-ion anisotropy) and the antisymmetric anisotropic part (the DM interaction) of the full exchange. In particular, we performed direct calculations on the magnetic M-M pairs parallel to the crystallographic a direction (Fig. 1), determining the exchange tensor reported in Eq. (A3). The interaction between the five other nearest-neighbor pairs can be evaluated via the three-fold rotational symmetry, as in Eq. (A4). In all our systems, the tensor turned out to be symmetric or, equivalently, any antisymmetric (DM-like) contribution was found to be negligible.

APPENDIX C: DETAILS OF NON-SPIN-POLARIZED HOPPING PARAMETERS

To understand the microscopic mechanisms dictated by symmetry considerations of the space group $P\bar{3}m1$ (164), it is insightful to first consider the underlying electronic processes, which we model with an effective tight-binding Hamiltonian reduced on the magnetic ions M. The corresponding Hamiltonian is given in Eq. (B3). The hopping parameters discussed in this section were obtained using the Full Potential Local Orbital [44] (FPLO) code within the generalized gradient approximation [39] (GGA) and served in the relativistic case as basis for the projED results in the main text.

1. Effects without spin-orbit coupling

We first consider the case without spin-orbit coupling effects. In this case, $t_{l\alpha,m\beta}^{\sigma\sigma'} = t_{l\alpha,m\beta}^{\sigma\sigma'} \delta_{\sigma\sigma'}$.

TABLE VI. Nonrelativistic, non-spin-polarized hopping parameters for a generic Z bond, considering only symmetry restrictions, as well as hopping parameters (in meV) for VCl_2 on a Z_1, Z_2, and Z_3 bonds as defined in Fig. 1. The dominant hoppings are highlighted for Z_1 (t_3, $\tilde{t}$), Z_2 (t_2, $\tilde{t}$) and Z_3 (t_3, t_5, t_6).

	generic Z bond					Z_1-bond VCl_2				
	d_{xy}	d_{xz}	d_{yz}	$d_{x^2-y^2}$	d_{z^2}	d_{xy}	d_{xz}	d_{yz}	$d_{x^2-y^2}$	d_{z^2}
d_{xy}	t_3	t_4	t_4	0	$\tilde{t}$	**−248**	10	10	0	**121**
d_{xz}	t_4	t_1	t_2	t_8	t_7	10	68	30	0	−3
d_{yz}	t_4	t_2	t_1	$-t_8$	t_7	10	30	68	0	−3
$d_{x^2-y^2}$	0	$-t_8$	t_8	t_5	0	0	0	0	−90	0
d_{z^2}	$\tilde{t}$	t_7	t_7	0	t_6	**121**	−3	−3	0	−2

	Z_2-bond VCl_2					Z_3-bond VCl_2				
	d_{xy}	d_{xz}	d_{yz}	$d_{x^2-y^2}$	d_{z^2}	d_{xy}	d_{xz}	d_{yz}	$d_{x^2-y^2}$	d_{z^2}
d_{xy}	1	−2	−2	0	**16**	**−19**	2	2	0	13
d_{xz}	−2	5	**−13**	2	2	2	2	−4	−2	−2
d_{yz}	−2	**−13**	5	−2	2	2	−4	2	2	−2
$d_{x^2-y^2}$	0	2	−2	−1	0	0	−2	2	**56**	0
d_{z^2}	**16**	2	2	0	1	13	−2	−2	0	**−20**

TABLE VII. Relativistic hopping parameters λ_ν (in meV) for VI_2 on-site and on a Z_1 bond as defined in Fig. 1, with $\nu \in \{x, y, z\}$ and $\mathcal{H}_{hop} = t_{ij}^{\alpha\beta} + \frac{i}{2}\vec{\lambda}_{ij}^{\alpha\beta} \cdot \vec{\sigma}$.

	on-site VI_2					Z_1-bond VI_2				
λ_z	d_{xy}	d_{xz}	d_{yz}	$d_{x^2-y^2}$	d_{z^2}	d_{xy}	d_{xz}	d_{yz}	$d_{x^2-y^2}$	d_{z^2}
d_{xy}	0	0	0	−31	0	0	−1	1	−17	0
d_{xz}	0	0	**−38**	2	0	1	0	−2	−1	−3
d_{yz}	0	**38**	0	2	0	−1	2	0	−1	3
$d_{x^2-y^2}$	31	−2	−2	0	−6	17	1	1	0	**36**
d_{z^2}	0	0	0	6	0	0	3	−3	**−36**	0
λ_x	d_{xy}	d_{xz}	d_{yz}	$d_{x^2-y^2}$	d_{z^2}	d_{xy}	d_{xz}	d_{yz}	$d_{x^2-y^2}$	d_{z^2}
d_{xy}	0	**−38**	0	−1	−2	0	−1	−12	1	−1
d_{xz}	**38**	0	0	0	−2	1	0	0	21	−1
d_{yz}	0	0	0	16	27	12	0	0	0	−2
$d_{x^2-y^2}$	1	0	−16	0	−6	−1	−21	0	0	1
d_{z^2}	2	2	−27	6	0	1	1	2	−1	0
λ_y	d_{xy}	d_{xz}	d_{yz}	$d_{x^2-y^2}$	d_{z^2}	d_{xy}	d_{xz}	d_{yz}	$d_{x^2-y^2}$	$d_{z^2}d_{xy}$
d_{xy}	0	0	38	−1	2	0	12	1	1	1
d_{xz}	0	0	0	16	−27	−12	0	0	0	2
d_{yz}	**−38**	0	0	−0	2	−1	0	0	21	1
$d_{x^2-y^2}$	1	−16	0	0	−6	−1	0	−21	0	1
d_{z^2}	−2	27	−2	6	0	−1	−2	−1	−1	0

Let us consider the symmetry restrictions on first, second and third neighbor bonds, which can be all described by the same reduced matrices due to $2/m$ symmetry at their bond center. For this discussion, we focus on Z_1, Z_2, and Z_3 bonds, which can be related to the other first, second, and third neighbor bonds by the appropriate symmetry operations of the crystal. The Z_1 and Z_3 bonds are parallel to the crystallographic a direction, in cubic coordinates along $[1\bar{1}0]$ and the corresponding C_2 rotation axis is parallel to the bond. The Z_2 bond is perpendicular to that bond, in cubic coordinates along the $[11\bar{2}]$ direction. Since in this case the C_2 axis is perpendicular to the bond and in-plane, it turns out to be parallel to the C_2 axes of the Z_1 and Z_3 bond and the same restrictions on the hopping matrices are valid in this case.

In Table VI, we list the generic hopping matrix on a Z bond with $2/m$ symmetry at the bond center. The hopping matrix between t_{2g} orbitals is fully determined by four parameters $t_{1,...,4}$, following the convention introduced in Ref. [86]. For a perfect octahedral geometry of the ligands $t_4 = 0$. In the materials considered, the octahedra do not deviate too strongly from a perfect shape, hence t_4 is generally small, as can be seen for the hopping parameters listed for the example case $NiCl_2$. Following from the Slater-Koster integrals in a 90° M-X-M geometry [42], t_2 is dominated by ligand-assisted hopping processes, while t_1 and t_3 arise mainly from direct hopping.

Hopping between t_{2g} and e_g orbitals is constrained to three parameters, $\tilde{t}$, t_7, and t_8. However, if the considered bond lies within a mirror plane, t_7 and t_8 vanish. While this is not a symmetry of the crystal, it is a symmetry of a single bond Ni_2I_{10} molecule. In the crystal, these hoppings are hence finite, but small. Consequently, the ligand-assisted $\tilde{t}$ dominates the exchange between t_{2g} and e_g orbitals.

Finally, hopping between e_g orbitals can be described with two parameters t_5 and t_6, where the off-diagonal terms vanish due to the $2/m$ symmetry. These hoppings turn out to

be important for further neighbor interactions on, e.g., the Z_3 bond.

2. Effects of spin-orbit coupling

As mentioned in the main text, the Hamiltonian $\mathcal{H}_{hop} = \sum_{lm} \sum_{\alpha\beta} \underline{c}_{l\alpha}^T \{t_{\alpha\beta}^{lm} \, \mathrm{I} + \frac{i}{2}(\vec{\lambda}_{\alpha\beta}^{lm} \cdot \vec{\sigma})\} \underline{c}_{m\beta}$ is suitable to describe hopping processes including spin-orbit coupling effects. In Table VII, we list for the example case VI_2 the hopping parameters on-site and for the Z_1 bond.

The on-site hopping parameters can be directly compared to the analytic expressions of the matrix elements in $\lambda_{eff} \mathbf{L} \cdot \mathbf{S}$ for d orbitals in the atomic limit:

λ_z	d_{xy}	d_{xz}	d_{yz}	$d_{x^2-y^2}$	d_{z^2}	
d_{xy}	0	0	0	$2\lambda_{eff}$	0	
d_{xz}	0	0	$-\lambda_{eff}$	0	0	
d_{yz}	0	λ_{eff}	0	0	0	(C1)
$d_{x^2-y^2}$	$-2\lambda_{eff}$	0	0	0	0	
d_{z^2}	0	0	0	0	0	

λ_x	d_{xy}	d_{xz}	d_{yz}	$d_{x^2-y^2}$	d_{z^2}	
d_{xy}	0	$-\lambda_{eff}$	0	0	0	
d_{xz}	λ_{eff}	0	0	0	0	
d_{yz}	0	0	0	$-\lambda_{eff}$	$-\sqrt{3}\lambda_{eff}$	(C2)
$d_{x^2-y^2}$	0	0	λ_{eff}	0	0	
d_{z^2}	0	0	$\sqrt{3}\lambda_{eff}$	0	0	

$$\lambda_y \begin{array}{c|ccccc} & d_{xy} & d_{xz} & d_{yz} & d_{x^2-y^2} & d_{z^2} \\ \hline d_{xy} & 0 & 0 & \lambda_{\text{eff}} & 0 & 0 \\ d_{xz} & 0 & 0 & 0 & -\lambda_{\text{eff}} & \sqrt{3}\lambda_{\text{eff}} \\ d_{yz} & -\lambda_{\text{eff}} & 0 & 0 & 0 & 0 \\ d_{x^2-y^2} & 0 & \lambda_{\text{eff}} & 0 & 0 & 0 \\ d_{z^2} & 0 & -\sqrt{3}\lambda_{\text{eff}} & 0 & 0 & 0 \end{array} \quad \text{(C3)}$$

As discussed in the main text, comparison to the values obtained for the monolayer structures (see Table VII for the example case VI_2) does not allow to identify one unique effective spin-orbit coupling strength λ_{eff}. This can be attributed to the fact that spin-orbit coupling effects arise mainly from the heavy ligand p elements (here I), not the metal d elements (here V).

The *ab initio* form of the on-site SOC terms allows for intuitive understanding on why the single-ion anisotropy contributes for NiX_2 compounds with heavy ligands, but always vanishes for VX_2. If SOC is treated perturbatively, SIA arises from mixing of spin multiplets of different total spin S. Assuming that excited levels with different occupancy of t_{2g} and e_g levels are too high in energy to be relevant, the analysis can be restricted onto SOC matrix elements of a given orbital subset. For the d^3 VX_2 compounds, the relevant SOC matrix elements are within the t_{2g} levels. As evident from the left column of Table VII, the SOC matrix elements within the t_{2g} levels do conform to a rotationally symmetric form of type $L_{\text{eff}} \cdot S$, where L_{eff} are effective $L = 1$ operators acting within the basis of (d_{xy}, d_{xz}, d_{yz}) orbitals. Intuitively, one would not expect them to induce strong SIA as they are rotationally symmetric themselves. In contrast, for the d^8 NiX_2 compounds the relevant orbital subset consists of the e_g levels. Here, the SOC matrix elements are of type $L_y \cdot S_c$, where
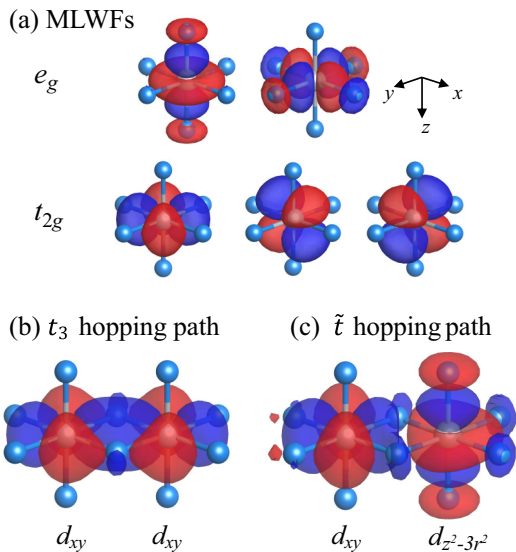

FIG. 5. DOS projected onto M-d and Cl-p orbital states for (a) $NiCl_2$, (b) VCl_2, and (c) $MnCl_2$. Fermi level is set at energy origin.

$S_c = (S_x + S_y + S_z)$, and L_y is an effective $L = 1/2$ operator in the basis of $(d_{x^2-y^2}, d_{z^2})$ orbitals. This operator is not rotationally symmetric. Therefore the induced SOC from ligand elements breaks rotational symmetry within the e_g orbitals, but not within the t_{2g} orbitals. We expect therefore induced SIA by heavy ligands in the d^8 Ni compounds, but not in the d^3 V compounds.

On a nearest-neighbor bond, one can assume that the crystal-field effects at the ligand site split the p levels, such that the p_z orbital is split off from the p_x and p_y. This suggests that the z component of the SOC at the ligand dominates the effect, which couples the p_x and p_y orbitals. In this case, the SOC at the ligand, when projected into the d-orbital Wannier functions, results in a complex hopping $\lambda^z_{(x^2-y^2;z^2)}$. A similar analysis of this situation was done in Ref. [31].

APPENDIX D: SPIN-POLARIZED WANNIER FUNCTION ANALYSIS

For completion, we discuss in this section spin-polarized nearest-neighbor hopping integrals to give further insight into the microscopic mechanism behind the magnetic couplings in the cases of monolayer MCl_2 (M=V, Mn, and Ni). After a DFT calculation was performed by using the VASP code [79] and GGA+U functional with $U = 1.8$ eV and $J_H = 0.8$ eV,

FIG. 4. (a) 3d-orbital MLWFs in VCl_6 octahedral coordination in VCl_2 monolayer. [(b) and (c)] Combination of MLWFs for t_3 and $\tilde{t}$ hopping paths in ferromagnetic configuration. Isosurface levels were set at $\pm 0.8 \, a_0^{-3/2}$. Blue and red colors show opposite signs of MLWF.
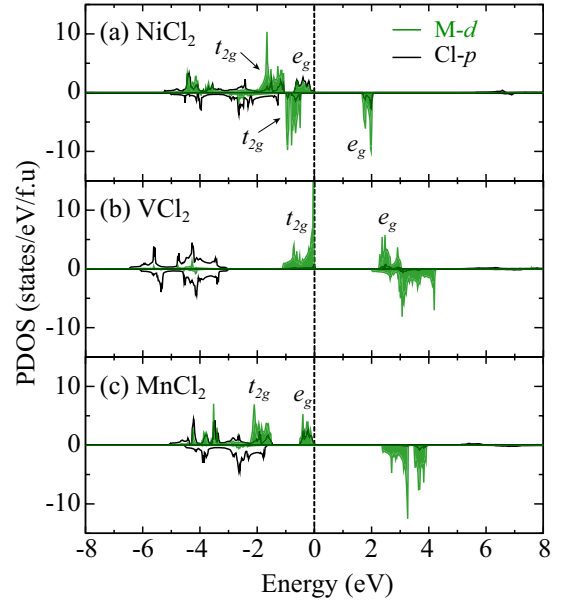
TABLE VIII. Hopping integrals t_{eff} calculated via spin-polarized MLWFs basis set for first nearest-neighbor coupling in ferromagnetic spin configuration.

	$NiCl_2$	VCl_2	$MnCl_2$
t_3	−77 meV	−250 meV	−81 meV
$\tilde{t}$	37 meV	−33 meV	0.5 meV

TABLE IX. Exchange parameters (in meV) for the MX_2 monolayer structures using $(U_{avg}, J_{avg}) = (1.8, 0.8)$ eV; extracted with the projED method (left) and the four-state energy mapping method (right).

	projED			four-state		
	$NiCl_2$	$NiBr_2$	NiI_2	$NiCl_2$	$NiBr_2$	NiI_2
J_1	-2.2	-2.1	-2.5	-5.1	-6.0	-8.0
K_1	0.0	$+0.1$	$+1.3$	0.0	$+0.2$	$+3.2$
Γ_1	0.0	0.0	0.0	0.0	0.0	$0.$
Γ_1'	0.0	0.0	-0.1	0.0	0.0	-0.2
J_2	-0.1	-0.1	-0.1	-0.1	-0.1	-0.3
J_3	$+1.2$	$+1.7$	$+2.4$	$+1.7$	$+2.9$	$+5.8$
A_c	0.0	$+0.1$	$+0.7$	0.0	0.0	$+0.6$
	projED			four-state		
	VCl_2	VBr_2	VI_2	VCl_2	VBr_2	VI_2
J_1	$+7.8$	$+5.0$	$+2.6$	$+8.6$	$+5.1$	$+1.8$
K_1	0.0	0.0	0.0	0.0	0.0	$0.$
Γ_1	0.0	0.0	0.0	0.0	0.0	$0.$
Γ_1'	0.0	0.0	0.0	0.0	0.0	$0.$
J_2	0.0	$+0.1$	$+0.1$	0.0	0.0	$+0.1$
J_3	0.0	$+0.1$	$+0.1$	-0.1	$+0.2$	$+0.3$
A_c	0.0	0.0	-0.1	0.0	$0.$	$0.$
	projED			four-state		
	$MnCl_2$	$MnBr_2$	MnI_2	$MnCl_2$	$MnBr_2$	MnI_2
J_1	$+1.2$	$+1.0$	$+0.9$	$+0.4$	$+0.3$	$+0.3$
K_1	0.0	0.0	0.0	0.0	0.0	$0.$
Γ_1	0.0	0.0	0.0	0.0	0.0	$0.$
Γ_1'	0.0	0.0	0.0	0.0	0.0	$0.$
J_2	0.0	0.0	$+0.1$	0.0	0.0	$+0.1$
J_3	$+0.1$	$+0.1$	$+0.1$	$+0.1$	$+0.1$	$+0.1$
A_c	0.0	0.0	0.0	0.0	$0.$	$0.$

the hopping parameter t_{dd}^{eff} between the transition-metal sites was extracted via the maximally localized Wannier functions (MLWFs) as constructed from projection of five transition-metal d states and six ligand p states [87]. The shapes of the d-orbital MLWFs are shown in Fig. 4(a). Note that the dp-pd hybridization process is implicitly included in t_{dd}^{eff} hopping since the Wannier function has delocalized character reflecting the hybridization with the surrounding ligands' p orbital

states. The orbital-dependent hopping integrals between the first nearest neighbor M sites were calculated in ferromagnetic spin configuration. A $\mathbf{k}$-point grid of $18 \times 18 \times 1$ in the two-dimensional Brillouin zone was used for all the calculations. $\mathbf{k}$-point integration in the Brillouin zone was done using the tetrahedron method with Blöchl corrections.

Figure 5 shows the density of states projected onto M-d and Cl-p orbital states. Strong hybridization between M-d and Cl-p orbitals can be seen in the cases of $NiCl_2$ and $MnCl_2$, but not in VCl_2, resultant from the different d electron filling. The CFS causes large band gap between e_g and t_{2g} orbital states in Ni minority-spin state and V majority-spin state.

As mentioned in Sec. III B, the nearest-neighbor exchange coupling can be explained by the hopping integrals between d_{xy} and d_{xy} orbitals and d_{xy} and d_{z^2} orbitals, namely, t_3 and $\tilde{t}$. Table VIII lists the calculated hopping parameters through the spin-polarized Wannier functions.

In $NiCl_2$, weak ferromagnetic exchange is attributed to $\tilde{t}$ ($= 37$ meV) hopping between filled $t_{2g}^{\downarrow}$ state and empty $e_g^{\downarrow}$ state. Since the t_{2g} state is fully occupied, t_3 hopping does not play any role in the exchange interaction.

In VCl_2, $t_{2g}^{\uparrow}$ state is fully occupied while $e_g^{\uparrow}$ state is empty. It is found that anti-parallel-spin-favored t_3 hopping is much stronger than parallel-spin-favored $\tilde{t}$ hopping. As shown in Figs. 4(b) and 5(c), t_3 hopping is direct d-d hopping while $\tilde{t}$ hopping is $dp(\sigma)$-$pd(\pi)$ indirect hopping. This result is consistent with what was discussed in Sec. III B.

In $MnCl_2$, d^5 electron fully occupies the majority spin state and opens a wide band gap. As being speculated, this leads to weak exchange interaction while $|t_3| \gg |\tilde{t}|$ condition results in antiparallel spin exchange interaction.

APPENDIX E: EXCHANGE PARAMETERS FOR ALTERNATIVE U_{avg} AND J_{avg} VALUES

To provide context of the dependence on the Coulomb repulsion U_{avg} and Hund's coupling J_{avg}, we list in Table IX the exchange parameters extracted with projED and the four-state method for $(U_{avg}, J_{avg}) = (1.8, 0.8)$ eV. These parameters were chosen previously by some of the authors [48,52] for the analysis of the NiX_2 materials.

Not surprisingly, the trends agree with the parameters listed in the main text in II to IV for the values determined with constrained RPA. The overall tendency toward larger absolute values in both methods can be assigned to the smaller Coulomb repulsion, which results in an overall increase of the magnetic exchange.

[1] A. P. Ramirez, Annu. Rev. Mater. Sci. **24**, 453 (1994).

[2] L. Balents, Nature (London) **464**, 199 (2010).

[3] *Introduction to Frustrated Magnetism*, edited by C. Lacroix, P. Mendels, and F. Mila, Springer Series in Solid-State Sciences Vol. 164 (Springer Science & Business Media, Berlin, 2011).

[4] O. A. Starykh, Rep. Prog. Phys. **78**, 052502 (2015).

[5] *Spintronic 2D Materials: Fundamentals and Applications*, edited by W. Liu and Y. Xu, Materials Today (Woodhead Publishing, 2019).

[6] *Low-Dimensional Magnetism*, edited by A. N. Vasiliev, O. S. Volkova, E. A. Zvereva, and M. M. Markina (CRC Press, 2019).

[7] S. M. Winter, Y. Li, H. O. Jeschke, and R. Valentí, Phys. Rev. B **93**, 214431 (2016).

[8] S. M. Winter, K. Riedl, P. A. Maksimov, A. L. Chernyshev, A. Honecker, and R. Valentí, Nat. Commun. **8**, 1152 (2017).

[9] H.-S. Kim and H.-Y. Kee, Phys. Rev. B **93**, 155143 (2016).

[10] R. Yadav, N. A. Bogdanov, V. M. Katukuri, S. Nishimoto, J. van den Brink, and L. Hozoi, Sci. Rep. **6**, 37925 (2016).

[11] Y. S. Hou, H. J. Xiang, and X. G. Gong, Phys. Rev. B **96**, 054410 (2017).

[12] C. Eichstaedt, Y. Zhang, P. Laurell, S. Okamoto, A. G. Eguiluz, and T. Berlijn, Phys. Rev. B **100**, 075110 (2019).

[13] P. Laurell and S. Okamoto, npj Quantum Mater. **5**, 2 (2020).

[14] J. L. Lado and J. Fernández-Rossier, 2D Mater. **4**, 035002 (2017).

[15] C. Xu, J. Feng, H. Xiang, and L. Bellaiche, npj Comput. Mater. **4**, 57 (2018).

[16] O. Besbes, S. Nikolaev, N. Meskini, and I. Solovyev, Phys. Rev. B **99**, 104432 (2019).

[17] I. Lee, F. G. Utermohlen, D. Weber, K. Hwang, C. Zhang, J. van Tol, J. E. Goldberger, N. Trivedi, and P. C. Hammel, Phys. Rev. Lett. **124**, 017201 (2020).

[18] A. Kartsev, M. Augustin, R. F. Evans, K. S. Novoselov, and E. J. G. Santos, npj Comput. Mater. **6**, 150 (2020).

[19] Y. O. Kvashnin, A. Bergman, A. I. Lichtenstein, and M. I. Katsnelson, Phys. Rev. B **102**, 115162 (2020).

[20] P. P. Stavropoulos, X. Liu, and H.-Y. Kee, Phys. Rev. Research **3**, 013216 (2021).

[21] A. Edström, D. Amoroso, S. Picozzi, P. Barone, and M. Stengel, Phys. Rev. Lett. **128**, 177202 (2022).

[22] S. Bandyopadhyay, F. L. Buessen, R. Das, F. G. Utermohlen, N. Trivedi, A. Paramekanti, and I. Dasgupta, Phys. Rev. B **105**, 184430 (2022).

[23] Y. Tokunaga, D. Okuyama, T. Kurumaji, T. Arima, H. Nakao, Y. Murakami, Y. Taguchi, and Y. Tokura, Phys. Rev. B **84**, 060406(R) (2011).

[24] T. Kurumaji, S. Seki, S. Ishiwata, H. Murakawa, Y. Kaneko, and Y. Tokura, Phys. Rev. B **87**, 014429 (2013).

[25] T. Kurumaji, S. Seki, S. Ishiwata, H. Murakawa, Y. Tokunaga, Y. Kaneko, and Y. Tokura, Phys. Rev. Lett. **106**, 167206 (2011).

[26] Y. Li, D. Chen, X. Dong, L. Qiao, Y. He, X. Xiong, J. Li, X. Peng, J. Zheng, X. Wang, *et al.*, J. Phys.: Condens. Matter **32**, 335803 (2020).

[27] Q. Song, C. A. Occhialini, E. Ergeçen, B. Ilyas, D. Amoroso, P. Barone, J. Kapeghian, K. Watanabe, Taniguchi, Takashi, A. S. Botana, S. Picozzi, N. Gedik, and R. Comin, Nature (London) **602**, 601 (2022).

[28] A. O. Fumega and J. L. Lado, 2D Mater. **9**, 025010 (2022).

[29] Z. Jiang, Y. Li, W. Duan, and S. Zhang, Phys. Rev. Lett. **122**, 236402 (2019).

[30] A. S. Botana and M. R. Norman, Phys. Rev. Materials **3**, 044001 (2019).

[31] P. P. Stavropoulos, D. Pereira, and H.-Y. Kee, Phys. Rev. Lett. **123**, 037203 (2019).

[32] K. Riedl, Y. Li, R. Valentí, and S. M. Winter, Phys. Status Solidi B **256**, 1800684 (2019).

[33] H. Xiang, C. Lee, H.-J. Koo, X. Gong, and M.-H. Whangbo, Dalton Trans. **42**, 823 (2013).

[34] X. Li, H. Yu, F. Lou, J. Feng, M.-H. Whangbo, and H. Xiang, Molecules **26**, 803 (2021).

[35] P. W. Anderson, Phys. Rev. **79**, 350 (1950).

[36] J. Kanamori, J. Phys. Chem. Solids **10**, 87 (1959).

[37] A. Kitaev, Ann. Phys. **321**, 2 (2006).

[38] S. M. Winter, A. A. Tsirlin, M. Daghofer, J. van den Brink, Y. Singh, P. Gegenwart, and R. Valentí, J. Phys.: Condens. Matter **29**, 493002 (2017).

[39] J. P. Perdew, K. Burke, and M. Ernzerhof, Phys. Rev. Lett. **77**, 3865 (1996).

[40] F. Aryasetiawan, M. Imada, A. Georges, G. Kotliar, S. Biermann, and A. I. Lichtenstein, Phys. Rev. B **70**, 195104 (2004).

[41] F. Aryasetiawan, K. Karlsson, O. Jepsen, and U. Schönberger, Phys. Rev. B **74**, 125106 (2006).

[42] *Correlated Electrons: From Models to Materials*, edited by E. Pavarini, E. Koch, F. Anders, and M. Jarrell, Schriften des Forschungszentrums Jülich: Modeling and Simulation Vol. 2 (Forschungszentrum Jülich GmbH, Institute for Advanced Simulation, 2012).

[43] H. Eschrig and K. Koepernik, Phys. Rev. B **80**, 104503 (2009).

[44] K. Koepernik and H. Eschrig, Phys. Rev. B **59**, 1743 (1999).

[45] A. Georges, L. d. Medici, and J. Mravlje, Annu. Rev. Condens. Matter Phys. **4**, 137 (2013).

[46] A. Abragam and B. Bleaney, *Electron Paramagnetic Resonance of Transition Ions* (Oxford University Press, Oxford, 2012).

[47] S. M. Winter, arXiv:2204.09856.

[48] D. Amoroso, P. Barone, and S. Picozzi, Nat. Commun. **11**, 5784 (2020).

[49] P. A. Lindgard, R. J. Birgeneau, H. J. Guggenheim, and J. Als-Nielsen, J. Phys. C: Solid State Phys. **8**, 1059 (1975).

[50] P. Day, A. Dinsdale, E. R. Krausz, and D. J. Robbins, J. Phys. C: Solid State Phys. **9**, 2481 (1976).

[51] J. Y. Ni, X. Y. Li, D. Amoroso, X. He, J. S. Feng, E. J. Kan, S. Picozzi, and H. J. Xiang, Phys. Rev. Lett. **127**, 247204 (2021).

[52] D. Amoroso, P. Barone, and S. Picozzi, Nanomaterials **11**, 1873 (2021).

[53] K. Katsumata and K. Yamasaka, J. Phys. Soc. Jpn. **34**, 346 (1973).

[54] D. Billerey, C. Terrier, A. J. Pointon, and J. P. Redoules, J. Magn. Magn. Mater. **21**, 187 (1980).

[55] C. Xu, J. Feng, M. Kawamura, Y. Yamaji, Y. Nahas, S. Prokhorenko, Y. Qi, H. Xiang, and L. Bellaiche, Phys. Rev. Lett. **124**, 087205 (2020).

[56] L. Régnault, J. Rossat-Mignod, A. Adam, D. Billerey, and C. Terrier, J. Phys. France **43**, 1283 (1982).

[57] E. Rastelli, A. Tassi, and L. Reatto, Physica B+C **97**, 1 (1979).

[58] K. Katsumata and M. Date, J. Phys. Soc. Jpn. **27**, 1360 (1969).

[59] S. Babu, K. Prokeš, Y. K. Huang, F. Radu, and S. K. Mishra, J. Appl. Phys. **125**, 093902 (2019).

[60] D. Billerey, C. Terrier, N. Ciret, and J. Kleinclauss, Phys. Lett. A **61**, 138 (1977).

[61] D. Billerey, C. Terrier, R. Mainard, and A. J. Pointon, Phys. Lett. A **77**, 59 (1980).

[62] S. R. Kuindersma, J. P. Sanchez, and C. Haas, Physica B+C **111**, 231 (1981).

[63] P. Day and K. R. A. Ziebeck, J. Phys. C: Solid State Phys. **13**, L523 (1980).

[64] A. Adam, D. Billerey, C. Terrier, R. Mainard, L. P. Regnault, J. Rossat-Mignod, and P. Mériel, Solid State Commun. **35**, 1 (1980).

[65] P. Day, M. W. Moore, T. E. Wood, D. M. Paul, K. R. Ziebeck, L. P. Regnault, and J. Rossat-Mignod, Solid State Commun. **51**, 627 (1984).

[66] K. Riedl, E. Gati, D. Zielke, S. Hartmann, O. M. Vyaselev, N. D. Kushch, H. O. Jeschke, M. Lang, R. Valentí, M. V. Kartsovnik, and S. M. Winter, Phys. Rev. Lett. **127**, 147204 (2021).

[67] M. Niel, C. Cros, G. Le Flem, M. Pouchard, and P. Hagenmuller, Physica B+C **86-88**, 702 (1977).

[68] H. Kadowaki, K. Ubukoshi, K. Hirakawa, J. L. Martínez, and G. Shirane, J. Phys. Soc. Jpn. **56**, 4027 (1987).

[69] H. Kadowaki, K. Ubukoshi, and K. Hirakawa, J. Phys. Soc. Jpn. **54**, 363 (1985).

[70] K. Hirakawa, H. Kadowaki, and K. Ubukoshi, J. Phys. Soc. Jpn. **52**, 1814 (1983).

[71] M. Nishi, Y. Ito, H. Kadowaki, and K. Hirakawa, J. Phys. Soc. Jpn. **53**, 1214 (1984).

[72] S. Kuindersma, C. Haas, J. Sanchez, and R. Al, Solid State Commun. **30**, 403 (1979).

[73] Physics division semiannual progress report for period ending September 10, 1954, Tech. Rep., Oak Ridge National Laboratory Report No. ORNL-1798, 1954.

[74] T. Sato, H. Kadowaki, and K. Iio, Phys. B: Condens. Matter **213-214**, 224 (1995).

[75] K. Iio, H. Masuda, H. Tanaka, and K. Nagata, J. Magn. Magn. Mater. **90-91**, 265 (1990).

[76] T. Sato and H. Kadowaki, Neutron scattering study of MnX$_2$ (X = Br, I), Tech. Rep. No. JAERI-M–93-228, 1993.

[77] J. Cable, M. Wilkinson, E. Wollan, and W. Koehler, Phys. Rev. **125**, 1860 (1962).

[78] O. I. Utesov and A. V. Syromyatnikov, Phys. Rev. B **95**, 214420 (2017).

[79] G. Kresse and J. Furthmüller, Phys. Rev. B **54**, 11169 (1996).

[80] M. A. McGuire, Crystals **7**, 121 (2017).

[81] H. Jiang, R. I. Gómez-Abal, X. Li, C. Meisenbichler, C. Ambrosch-Draxl, and M. Scheffler, Comput. Phys. Commun. **184**, 348 (2013).

[82] Y. Yekta, H. Hadipour, E. Şaşıoğlu, C. Friedrich, S. A. Jafari, S. Blügel, and I. Mertig, Phys. Rev. Materials **5**, 034001 (2021).

[83] A. I. Liechtenstein, V. I. Anisimov, and J. Zaanen, Phys. Rev. B **52**, R5467(R) (1995).

[84] H. Liu and G. Khaliullin, Phys. Rev. B **97**, 014407 (2018).

[85] S. M. Winter, K. Riedl, and R. Valentí, Phys. Rev. B **95**, 060404(R) (2017).

[86] J. G. Rau, E. K.-H. Lee, and H.-Y. Kee, Phys. Rev. Lett. **112**, 077204 (2014).

[87] T. P. T. Nguyen, K. Yamauchi, T. Oguchi, D. Amoroso, and S. Picozzi, Phys. Rev. B **104**, 014414 (2021).